

# A 3D finite element model of ventral furrow invagination in the *Drosophila melanogaster* embryo

Vito Conte<sup>a</sup>, José J Muñoz<sup>b</sup>, Mark Miodownik<sup>a,\*</sup>

<sup>a</sup>*Materials Research Group, Div. Engineering, King's College London, UK*

<sup>b</sup>*Dep. of Appl. Mathematics III. Univ. Polit. Catalonia, Barcelona, Spain*

---

## Abstract

Ventral furrow formation is the first large-scale movement in the *Drosophila* cellular blastoderm which involves the co-ordinated shape change of cells, and as such is an ideal system to use as a proof of principle for simulation methods to study the mechanics of morphogenesis. We have developed a 3D finite element method model of ventral furrow formation by decomposing the total deformation into two parts: an imposed active deformation, and an elastic passive deformation superimposed onto the latter. The model imposes as boundary conditions (i) a constant yolk volume and (ii) a sliding contact condition of the cells against the vitelline membrane, which is interpolated as B-Spline surface. The active deformation simulates the effects of apical constriction and apico-basal elongation of cells. This set of local cellular mechanisms leads to global shape changes of the embryo which are associated with known gene expressions. Using the model we have tested different plausible mechanical hypotheses postulated to account for the observed invagination process. In particular, we conclude that only certain combinations of local cell shape change can successfully reproduce the invagination process. We have quantitatively

compared the model with a 2D model and shown that it exhibits a more robust invagination phenomenon. The 3D model has also revealed that invagination causes a yolk flow from the central region to the anterior and posterior ends of the embryo, causing an accordion-like global compression and expansion wave to move through the embryo. Such phenomenon cannot be described by 2D models.

*Key words:* invagination, *Drosophila*, finite elasticity, finite elements, gastrulation, active forces.

---

## 1 Introduction

In the last twenty years it has been shown that biomechanics plays an important role in the formation, repair and function of bones, organs and arteries (Holzapfel, 2000; Taber, 2004). Clearly biomechanics plays an equally important role at the scale of the cell and the scale of the embryo, and it is becoming clear that the contribution that mechanical modelling can make to understanding biological systems at these scales is both vital and timely. This topic is the subject of this paper: more specifically computer simulations of an important model biological system, morphogenesis in *Drosophila* embryos .

Although there is a detailed understanding of the molecular mechanisms underlying developmental patterning (Costa et al., 1994; Leptin, 1999), little is known about the process by which genetic information is translated via mechanics into physical form. Historically, efforts to study morphogenesis have been limited by the theoretical and technical difficulties of measuring, modelling and perturbing relevant forces and material properties in living systems. The first stages of embryonic development of *Drosophila* involve the

---

\* Corresponding Author: Tel. +44 (0) 20 7848 2442, Fax: +44 (0) 20 7848 2932

*Email address:* [mark.miodownik@kcl.ac.uk](mailto:mark.miodownik@kcl.ac.uk) (Mark Miodownik ).

*URL:* <http://www.kcl.ac.uk/materials/mam/> (Mark Miodownik ).

formation of the epithelium, (external layer of cells in the blastoderm that surrounds the yolk). Subsequently, these cells undergo a set of major changes in shape and topology, namely invagination on the ventral side and at the posterior end, which gives rise to the mesoderm and midgut (Leptin, 1995). The genetic control of the ventral invagination has been associated with the *snail* and *twist* genes that define the region involved and control the initiation of the signalling pathway (Parks and Wieschaus, 1991; Costa et al., 1994; Leptin, 1995). The kinematics of invagination is characterised by the apical flattening and subsequent apical constriction of the cells in the ventral area (Sweeton et al., 1991; Leptin and Grunewald, 1990; Kam et al., 1991). Eventually, these cells undergo apico-basal elongation, and later shortening, resulting in the invagination sequence shown in Fig. 1. The cell shaping during this process can thus be regarded simplistically as the contribution of two main, localised deformation modes: (i) apical constriction (wedging), and (ii) apical-basal elongation (columnarisation), resulting in bending of the epithelium (Sweeton et al., 1991; Leptin and Grunewald, 1990; Kam et al., 1991; Muñoz et al., 2007).

Although there is a great deal known about the genetics of the invagination process (Leptin, 1995; Hacker and Perrimon, 1998; Nikolaidou and Barrett, 2004; Dawes-Hoang et al., 2005), the mechanics is less well studied. This is partly due to a lack of appropriate experimental tools, but also because the paradigm of modelling biological systems through the construction of gene pathways is not readily compatible with a mechanical approach. Despite this, the importance of stress is being gradually investigated, especially in regulatory role of certain gene expressions (Gordon, 1999; Farge, 2003; Brouzés et al., 2004; Supatto et al., 2005).

There have been a number of 2D mechanical models proposed to study invagination (Taber, 1995). In the early work of Odell et al. (1981), trusses are located in cells which are controlled by a viscoelastic constitutive law that triggers their apical constriction, and a bistable mechanism that ensures the invagination process. Davidson et al. (1995)

also tested a global mechanism formed by a continuous microfilament ring around ventral cells that contracts the ventral cells. Other mechanical hypothesis include either (i) interactions in the junctions between the cell layer (cell tracting of plasma membrane (Jacobson et al., 1986)), (ii) interactions cell-extracellular matrix (ECM) such as peripheral intercalation, tangential forces (Clausi and Brodland, 1993; Brodland and Clausi, 1994) or cell crawling on ECM (Davidson et al., 1995), or (iii) external mechanisms such external forces (Clausi and Brodland, 1993; Brodland and Clausi, 1994) or swelling of apical lamina that forces the ECM to bend, (Davidson et al., 1995).

Recently Muñoz et al. (2007) developed a 2D finite element method (FEM) model of ventral furrow formation. In this work a deformation gradient decomposition method was used to model the permanent (active) deformations and the (passive) hyperelastic deformations as a local quantity applied to the continuum that schematises the epithelial layer. No structural elements such as rods were introduced and each point of the epithelial cell layer was treated as being able to produce any of the two main deformation modes involved in invagination: apical constriction and apico-basal cell elongation. These mechanisms were associated with known gene expressions and so in this way the mechanics was linked to known genetic pathways in a self-consistent manner throughout the whole embryo. One advantage of the method is the independence of the final deformed configuration from the material properties, for which there is at present very little information.

In this paper we extend this work to develop, to the authors knowledge, the first 3D model of ventral furrow invagination and explore the extent to which dimensionality is important in understanding the phenomenon. This aspect of the phenomenon is not only of interest to the theoreticians, but also to experimentalists because, at present, 3D imaging of embryos is difficult and so much attention is often paid to 2D sections when investigating the phenomenon. Thus the extent to which 3D nature of a real embryo determines mechanical phenomena such as ventral furrow formation is a very pertinent

question, which we address in this paper.

In the model there are no external constraints, other than the presence of the vitelline membrane and the yolk. The former is modelled as a rigid sleeve shaped shell constraining the deformation, and the latter imposes a constant volume constraint to the volume within the epithelium. The sliding contact condition is numerically modelled in a different manner to that reported in Muñoz et al. (2007). Here, we avoid the numerical instabilities (more critical in 3D analysis) by discretising the vitelline membrane with smooth B-Splines (Muñoz, 2007), and hence no faceted surfaces are obtained.

In describing the 3D model, we note that as in the 2D model, the causes of the active deformations are not specified. These are considered here as an internal (genetically or chemomechanically transduced) contribution that produce different combinations of the two active shape changes. A condition we intent to relax in future work.

## 2 Method

### 2.1 Deformation gradient decomposition method

We use a deformation gradient decomposition to model the active mechanisms governing ventral furrow invagination. This method is described fully and in detail in our previous paper (Muñoz et al., 2007), which describes our 2D investigations of the phenomena, thus in this section, we will limit ourselves to a brief overview of the method.

We denote by  $\boldsymbol{x}$  the current position of a material point, and by  $\boldsymbol{X}$  its reference position. We additionally introduce an intermediate configuration  $\bar{\boldsymbol{x}}$ , which is the result of applying an active deformation field given by  $\boldsymbol{F}_a = \frac{\partial \bar{\boldsymbol{x}}}{\partial \boldsymbol{X}}$  (Bonet and Wood, 1997; Taber, 2004). The deformation between configurations  $\boldsymbol{x}$  and  $\bar{\boldsymbol{x}}$  is assumed to be hyperelastic, and so the

elastic deformation gradient can be expressed as  $\mathbf{F}_e = \frac{\partial \mathbf{x}}{\partial \mathbf{x}_a}$ . Hence, the total deformation gradient  $\mathbf{F}$  is split resorting to a multiplicative decomposition with the form  $\mathbf{F} = \mathbf{F}_e \mathbf{F}_a$ . Fig. 2 illustrates these mappings and shows that the elastic deformation accounts for the compatibility of the deformation.

We use a simple Neo-Hookean hyperelastic model for the material, which has the following expression for the non-linear strain energy function  $\Psi$ :

$$\Psi = \frac{\mu}{2}(\mathbf{F}_e : \mathbf{F}_e - 3) - \mu \ln J_e + \frac{\lambda}{2}(\ln J_e)^2, \quad (1)$$

where  $J_e = \det(\mathbf{F}_e)$ ,  $\lambda = \frac{\nu E}{(1-2\nu)(1+\nu)}$  and  $\mu = \frac{E}{2(1+\nu)}$ . Elastic equilibrium, and therefore  $\mathbf{F}_e$ , is obtained by minimising the integral of this energy function in the whole domain of the embryo.

These imposed active deformations imply the presence of an energy source within the cells. We say nothing about the intensity of this energy source except that it exists and appears to produce the observed active cell shape changes, which are those actively imposed on the model by increasing them linearly proportional to a pseudo-time  $\tau$ .

## 2.2 Constructing the 3D Model of the Embryo

The 3D geometry was built by capturing the average external geometric shape of an embryo derived from experiment and building the internal structure using AutoCAD. Experimental evidence shows that the average length of a *Drosophila* embryo is of  $500\mu\text{m}$  with 2D cross sections almost circular with an average diameter of  $180\mu\text{m}$  (Grumbling et al., 2006); therefore, we used this observation to justify building an exact circular cross-section into the 3D geometry of the model. Since ventral furrow invagination begins just

after cellularisation has been completed, we consider the epithelial layer to have uniform thickness, with all of its cells being of the same size (although cells are not specifically modelled). In the center of the embryo is the yolk which we model as a boundary condition and not as a material, this is described later. Fig. 3 shows the main views and sections of the model embryo.

The volume of the cell layer was separated into different main regions: the mesoderm, the ectoderm, the anterior and the posterior cells, see Fig. 3.a-c. The mesoderm and ectoderm in the finite element model are the active regions, capable of exerting active stresses by changing shape elastically, whereas the anterior and posterior are modelled solely as passive elastic regions.

### 2.3 Active strains

In order to simulate the large deformations observed in the invagination process, the 3D material geometry has to undergo finite deformations that are modelled as local quantities applied to the continuum. According to such a description, any point in the epithelial cell layer of the 3D material geometry of the embryo is allowed to contribute to the global deformation; consequently, as in the 2D model, we circumvent the detailed modelling of the cytoskeleton with structural elements such as rods, trusses or ropes.

Following a common practice in finite element discretisation, we use the parent domain of each element (with parametric co-ordinates  $\boldsymbol{\xi}$ ) to express quantities in the reference configuration (with material co-ordinates  $\boldsymbol{X}$ ) (Bonet and Wood, 1997). We apply the field of active deformation  $\boldsymbol{J}_a$  onto the common parent domain, which results in a new set of stretched parametric co-ordinates  $\bar{\boldsymbol{\xi}}$  (see Fig. 2). The transformation  $\boldsymbol{J}_a = \frac{\partial \bar{\boldsymbol{\xi}}}{\partial \boldsymbol{\xi}}$  from  $\boldsymbol{\xi}$  to  $\bar{\boldsymbol{\xi}}$  has associated an equivalent active deformation gradient from the reference configuration  $\boldsymbol{X}$  to the intermediate configuration  $\bar{\boldsymbol{x}}$ , which is denoted by  $\boldsymbol{F}_a$  and it is such

that  $d\bar{\mathbf{x}} = \mathbf{F}_a d\mathbf{X}$ . After making use of the tangent map  $\mathbf{J}_\xi = \frac{\partial \xi}{\partial \mathbf{X}}$ , the active deformation gradient  $\mathbf{F}_a$  can be expressed as (see Fig. 2),

$$\mathbf{F}_a = \mathbf{J}_\xi^{-1} \mathbf{J}_a \mathbf{J}_\xi \quad (2)$$

We now define two transformations that represent apical constriction and apico-basal elongation of the parametric domain as follows:

$$\mathbf{J}_{ac}(\omega_{ac}) = \begin{bmatrix} 1 + \xi_2 \omega_{ac} & \xi_1 \omega_{ac} & 0 \\ 0 & 1 & 0 \\ 0 & 0 & 1 \end{bmatrix} \quad ; \quad \mathbf{J}_{el}(\omega_{el}) = \begin{bmatrix} 1 + \omega_{el} & 0 & 0 \\ 0 & \frac{1}{1 + \omega_{el}} & 0 \\ 0 & 0 & 1 \end{bmatrix} . \quad (3)$$

Both expressions of these transformations are written as a function of two parameters,  $\omega_{ac}$  and  $\omega_{el}$ , which represent the strength of these active deformations. The introduction of the pseudo-time  $\tau$  together with the linear pseudo-temporal dependence  $\omega_{ac}(\tau)$  and  $\omega_{el}(\tau)$  allow the explicit application of these active deformations to the geometry, thus replacing the action of the potential energy source. Modelling invagination using these parameters involves applying the different active deformations in different parts of the embryo.

Apico-basal shortening (see Fig. 4.a) is controlled by  $\omega_{el}(\tau)$  and is applied to the ectodermal regions ( $\omega_{el} < 0$ ) shown in Fig. 3.b. Apical constriction (Fig. 4.b) is controlled by  $\omega_{ac}(\tau)$  and is applied to the mesodermal regions shown in Fig. 3.a, to which an apico-basal elongation is also applied using  $\omega_{el} > 0$  (Fig.4.c). For  $\omega_{ac} = \omega_{el} = 0$  in either the mesoderm and the ectoderm no active deformation is applied. We note that in all the

applied deformations, the volume of the parametric domain is conserved (Muñoz et al., 2007).

#### 2.4 Implementing Constraints and Contact

The yolk of the embryo is a fluid which fills the region enclosed by the epithelial layer and plays an important role in invagination. The question of whether the yolk remains constant volume  $V$  throughout gastrulation (incompressibility of the fluid) or whether there is a residual pressure at the start of the invagination still remains unresolved experimentally. Certainly, it is a common observation that the yolk squirts out when the embryo is pierced before or during gastrulation. Therefore, we opted to implement both constancy and initial pressure of the yolk volume in order to analyse the effects due to the separation and the coupling of both.

We numerically enforced these two effects resorting to a penalty method where the total elastic potential of the epithelium  $\Pi_{EL}$  is complemented with an extra potential in the following way:

$$\Pi_{TOT} = \Pi_{EL} + \frac{p}{2}(V_y - (1 + f)V_{yo})^2 \quad (4)$$

where  $V_{yo}$  is the initial total volume of the yolk,  $p$  is a penalty parameter and  $f$  is a volume fraction factor. Constant pressure is emulated by forcing the yolk region to increase its volume by the fraction  $f$  during all the steps of the computer simulation. The parameter  $p$  controls the satisfaction of the constraint  $V_y = (1 + f)V_{yo}$ . The yolk volume  $V_y$  is computed by making use of the divergence theorem,

$$V_y = \int_V dv = \int_V \frac{1}{3} \text{div}(\mathbf{r}) dv = \frac{1}{3} \int_{\Gamma} \mathbf{r} \cdot \mathbf{n} ds. \quad (5)$$

where  $\mathbf{n}$  is the external normal of the volume boundary, and  $\mathbf{r}$  is the position vector of the boundary  $\Gamma$ . This method is computationally efficient in that it ensures minimal variations of the yolk volume whilst not requiring the numerical complexities of treating the yolk as a fluid. However, the actual value of  $p$  that ensures the satisfaction of the constraint depends on the stiffness of the embryo. In all our analyses, the choice of  $p$  in each case yielded volume variations less than 3.5%.

We represent the vitelline membrane as a rigid external shell that surrounds the embryo, see Fig. 3d. This requires the model to be able to simulate sliding contact conditions of the apical side of the cells onto this membrane. From the numerical standpoint, as in our 2D model, this contact phenomenon is treated via the use of the null space method (or master-slave approach (Muñoz and Jelenić, 2004)), which avoids Lagrange multipliers or penalty methods and uses only the minimum set of degrees of freedom. The faceted nature of finite element discretised surfaces gives rise to another problem when considering sliding, namely the discontinuity of the tangents. This gives rise to intermittent activation of the constraints, or so called ‘chatter’, which means that it is problematic to determine the suitable set of active constraints. For this reason, in this model, we used a cubic  $C^1$  continuous B-Spline interpolation smoothing technique on the contact surfaces (Muñoz, 2007). The technique is applied in conjunction with the null space method, where the solution is searched in an unconstrained manifold. The resulting formulation eases the contact transition along the master surface, and recovers the quadratic convergence of the iterative Newton-Raphson process. The method is far more robust for unilateral contact situations such as those treated here.

### 3 Numerical Experiments and Results

We performed a systematic series of simulations to investigate the influence on invagination of (i) the two types of active deformation modes (apical constriction or apico-basal elongation), and (ii) boundary conditions such as the internal presence of the yolk and the external presence of the rigid vitelline membrane. In each simulation, the initial undeformed configuration of the embryo is the one shown in Fig.4f.

Since the displacements are in general smooth, we have meshed the embryo so that the element size is inversely proportional to the local deformation of the embryo. We note though that while the radial elongation is independent of the mesh size, apical constriction is dependent on the radial discretisation. In order to consistently reproduce apico-basal deformations of a cell, no divisions were therefore employed along the radial thickness of the embryo.

#### 3.1 3D $\alpha$ study of invagination

In these simulations we apply the active deformation  $\mathbf{J}_a(0, -\omega_{el})$  in the ectoderm, which corresponds to radial shortening (tangential expansion) of the ectodermal elements (see Fig. 3b). Simultaneously we apply the active deformation  $\mathbf{J}_a(\omega_{ac}, \omega_{el})$  in the mesoderm (see Fig. 3.a), which corresponds to radial elongation and apical constriction of the mesodermal elements. Both deformations, in the ectoderm and in the mesoderm, are characterised by parameters  $\omega_{el}$  and  $\omega_{ac}$ . To simplify the analysis, in each simulation we adopted a constant ratio (with respect to  $\tau$ ) between  $\omega_{el}$  and  $\omega_{ac}$ , i.e. we used,

$$\alpha = \frac{\omega_{ac}}{\omega_{el}} = \text{constant}. \tag{6}$$

The value of  $\alpha$  is uniform all over the mesodermal domains as well as over the ectodermal domains. Clearly  $\alpha$  is uniformly equal to zero in the ectodermal regions, since there  $\omega_{ac} = 0$ . A set of numerical tests were performed for  $\alpha = 1, \dots, 12$  and  $+\infty$  ( $\omega_{el} = 0$ ) for the case when both ectoderm and mesoderm are active, and both the yolk and the vitelline constraints are present. Fig.5 shows a series of deformations at different steps of the pseudo-time when  $\alpha = 4$ . Fig. 6 shows the final invaginated state of the embryo for different values of  $\alpha$ .

The first observation is that the character of the invagination in the model depends on the relative magnitude of  $\alpha$ . A comparison of Fig. 6 with Fig. 1 makes it clear that for  $\alpha < 3$  the two borders of the ventral furrow remain too open to produce functional invagination and a large indented area is formed by the mesodermal cells. The same difficulties to close the furrow is encountered for values of  $\alpha > 6$ . In this case, though, a small cavity is created even if the wedge shaped ventral cells are highly constricted. We note that when the analyses were run for  $\alpha > 12$ , no substantial deformed configurations were obtained.

### *3.2 Constant $\alpha$ : The effect of constraints and other mechanisms*

Having varied  $\alpha$  we now tested the model in the case where  $\alpha$  is constant but other aspects of the model are changed. We tested the effect of removing the vitelline layer, of varying or removing the yolk pressure and finally of removing ectodermal pushing (using  $\omega_{el} = 0$  only in the ectodermal regions). Fig.7 shows the obtained deformations for the three conditions with  $\alpha = 4$ , corresponding to  $\omega_{ac} = 0.72$  and  $\omega_{ac} = 1.14$ . What is clear from these experiments is that the yolk, the vitelline layer and the ectodermal activity all have an important influence on the phenomenon of invagination. Using other values of  $\alpha$  produced similar results and did not produce any plausible invaginated phenotypes.

We performed further tests to investigate the effect of internal volume increased/decreased

by up to 2.5% of the initial yolk volume. Such pressure effects caused stress variations of up to 40% in the circumferential component in the epithelial layer, but no variations in the final deformed configurations.

### 3.3 *Material stiffness*

In most of the simulations we used  $E = 1000$  Pa and  $\nu = 0.3$  (Davidson et al., 1999). In order to detect any material dependence, material constants  $\lambda$  and  $\mu$  with different orders of magnitude were employed but we found that counter-intuitively deformed configurations are very similar regardless of the values used. This is due to the fact that the applied active deformations are independent of the stresses. The data are not shown here, but same effect was shown in the 2D model (Muñoz et al., 2007).

## 4 **Discussion**

### 4.1 *Discussion of plausible invagination mechanisms*

A comparison of Fig. 1 and Fig.5 shows that model closely reproduces the basic aspects of ventral furrow invagination. It confirms theoretical predictions that a combination of ectodermal pushing and mesoderm wedging are sufficient to cause invagination.

Earlier 2-D work (Muñoz et al., 2007) predicted that yolk volume and the presence of the vitelline layer would have a significant impact on invagination. In this work we confirmed those predictions in 3-D. Figs. 7 show the influence of the rigid vitelline membrane on invagination when  $\alpha = 4$ . It can be observed that the vitelline membrane clearly plays an important role in constraining the active deformation in both the intermediate and the final invaginated states. This is supported by the fact that removal of the vitelline

membrane results in the opening of the furrow in a gastrulating embryo *in vivo* (Leptin and Grunewald, 1990).

In addition we tested the impact of removing the internal yolk. Fig.7.c-d. shows a typical phenotype obtained, which shows that although invagination is successful, the intermediate and final state differs markedly from those obtained using the same active forces in the presence of yoke. We also investigated the effect of changing the pressure exerted by the yoke in invagination, this had little effect except for changing the stress concentrations in the epithelial layer. We can then conclude that in the model, although the volume constraint of the yolk plays an important role and affects the level of indentation of the invaginated region, small variations of the internal pressure have little phenotypic impact.

We also investigated the role of the ectoderm tangential pushing (radial shortening) in determining the in-folding of the mesodermal area, by simply switching off the active deformations ( $\omega_{el} = 0$ ) in the ectodermal regions (see Fig. 3b). The simulations were carried out to test the hypothesis that ectodermal pushing is not required for invagination (Leptin, 1995). However our results indicate that it is required, at least in the absence of any other invagination mechanism than those modelled here, namely mesodermal lengthening and wedging, as Figs.7e-f clearly show.

#### 4.2 3D - 2D Comparison

Many of the features in the 3D simulations were also observed in our previous 2D model (Muñoz et al., 2007). It is therefore pertinent to ask what features of the phenomenon are dimensionally dependant. This is especially important not only because the experimental system is 3D, but also because 2D images are frequently used to analyse the phenomenon, due to the difficulties in imaging in 3D.

In both the 2D and 3D model we found a range of values of  $\alpha$  that produced ventral furrow invagination which contained the acceptable basic features from the experimental biological viewpoint. But a more detailed quantitative analysis of phenomenon requires the quantification of invagination. Such an analysis is also necessary to quantitatively compare 2D and 3D invagination. Fig. 8 shows a comparison of a 2D furrow and a cross-section of the 3D furrow at the mid-point between the anterior and the posterior pole. It also shows a schematic showing our attempt to define measurable parameters which can define invagination, namely two quantities  $h$  (the height of the invagination pick at the ventral side) and  $g$  (the furrow-span at the ventral side) when final invagination is obtained. Fig. 9 shows how the ratio of  $h$  and  $g$  varies with  $\alpha$  for both the 2D and 3D models.

We note, that the characteristic quantities  $h$  and  $g$  in the central regions of the 3D model are acceptable for ranges from  $\alpha = 3$  to  $\alpha = 6$  (see Fig. 9). The data outside this interval (shown by non-filled symbols) denote phenotypes with an incomplete ventral furrow, see Fig. 6. A similar trend is shown in the 2D model, however it only produces acceptable invagination in the smaller interval  $4 \leq \alpha \leq 5$ . In other words there is a greater range of values of  $\alpha$  which reproduce the basic features of invagination in 3D model than in the 2D model. This leads us to conclude that 3D ventral furrow formation appears much more robust with respect to the variations of  $\alpha$ , (corresponding to variations in combinations of active stress mechanisms). In the absence of experimental measurements of  $h$  and  $g$  we can say no more at this stage, except to state that this quantitative measure of robustness could in principle be measured in experimental systems.

Another difference between the 2D and 3D model is the constancy of the yolk volume in a particular section of the embryo. In the 2D model there is only one possible section, and the yolk volume is constant. But in the 3D model although yolk volume is kept constant in the embryo as a whole, there is an extra degree of freedom allowing yolk to ‘flow’ around

the embryo which has the practical effect of allowing the yolk area of the many possible 2D cross-sections to vary. When we measured the yolk areas of different sections we found several interesting trends. Fig.10 a. shows a schematic of the sections we measured. Fig.10 b. shows a plot of the yolk areas at these points along the embryo during invagination. It can clearly be seen that the mid sections decrease in area and the posterior sections increase in area showing that there is yolk ‘flow’ from the middle of the embryo to the posterior (the effect is symmetrical, yolk also flows to the anterior). It should be stressed that this ‘flow’ is not modelled as such, it is inferred as a flow as a way to interpret the changes in cross-section areas of the yolk (redistribution of yolk volume).

An interesting feature is that the flow is non-linear and indeed there appears to be a net increase in total area (summed over all sections) in the early stages of invagination. This seemingly non-physical result is due to the fact that the embryo is changing shape (compressing along the anterior-posterior axis) and so the sections are becoming closer together, as shown when they are plotted in Fig.10c. Later in the process, the embryo expands and which can be seen in sinusoidal functional form of both the areas and section distances. Note also that different parts of the embryo expand at different times despite the fact that all active forces are applied at the same time. These motions are co-ordinated however, producing a characteristic ‘accordion’ wave of expansion along the embryo as seen Fig.10b.

The compression and expansion of the embryo and corresponding yolk flow appears to be a characteristic feature of invagination. It cannot be observed in 2D model since it is entirely a 3D effect. It is consistent with experimental evidence although no quantitative measurements have been performed to date. Such predictions provide a quantifiable and experimentally tractable way to test the model and thus our understanding of the mechanics of ventral furrow invagination.

## 5 Conclusions

We have developed a 3D finite element model of ventral furrow formation by decomposing the total deformation into two parts: an imposed active deformation, and a superimposed elastic passive deformation. The model uses the incompressible yolk and the rigid vitelline membrane as boundary conditions.

The active deformation simulates the effects of apical constriction and apico-basal elongation of cells. This set of local cellular mechanisms leads to global shape changes of the embryo which are associated with known gene expressions. We have tested different plausible mechanical hypotheses to account for the mechanical basis of ventral furrow invagination and show that ectodermal pushing is required for invagination when mesodermal wedging is the only other active mechanism present. We also confirmed the results of earlier 2D studies that show that the vitelline layer and yoke play an important role in ventral furrow invagination.

We have compared the 3D and 2D model, and from the evolution of the two geometric parameters  $h$  and  $g$ , we observe that invagination in the 3D model is less sensitive to the variations of  $\alpha$ , showing that the 3D model is more robust than the 2D model do fluctuations in the active stress.

The 3D model has revealed that invagination causes a yolk flow from the central region to the anterior and posterior ends of the embryo, this causes global compression and expansion of the embryo, the dynamics of which resemble the motion associated with an accordion. Such phenomena cannot be described by 2D models.

## 6 Acknowledgements

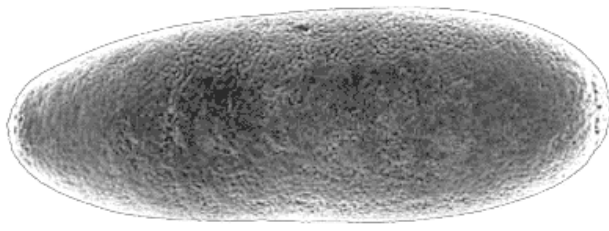
We would like to thank Buzz Baum for his helpful discussions and suggestions, Jue Tao for her initial 3D work. Jose Muñoz is financially supported by the Spanish Research Program Juan de la Cierva and Vito Conte is supported by the Biological and Physical Sciences Research Council (BBRSC). This support is greatly acknowledged.

## References

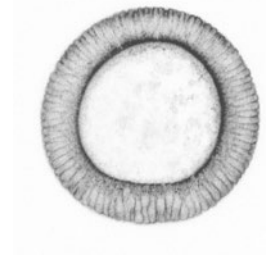
- Bonet, J., Wood, R., 1997. Non-linear continuum mechanics for finite element analysis. Cambridge University Press.
- Brodland, G. W., Clausi, D. A., 1994. Embryonic Tissue Morphogenesis Modeled by FEM. J. Biomech. Engin. 116, 146–155.
- Brouzés, E., Supatto, W., Farge, E., 2004. Is mechano-sensitive expression of twist involved in mesoderm formation? Biol. Cell 96, 471–477.
- Clausi, D. A., Brodland, G. W., 1993. Mechanical evaluation of theories of neurulation using computer simulations. Development 118, 1013–1023.
- Costa, M., Wilson, E., Wieschaus, E., 1994. A putative cell signal encoded by the folded gastrulation gene coordinates cell shape changes during *Drosophila* gastrulation. Cell 76 (6), 1075–89.
- Davidson, L. A., Koehl, M. A. R., Keller, R., Oster, G. F., 1995. How do sea urchins invaginate? Using biomechanics to distinguish between mechanisms of primary invagination. Development 121, 2005–2018.
- Davidson, L. A., Oster, G. F., Keller, R., Koehl, M. A. R., 1999. Measurements of Mechanical Properties of the Blastula Wall Reveal Which Hypothesized Mechanisms of Primary Invagination Are Physically Plausible in the Sea Urchin *Strongylocentrotus purpuratus*. Dev. Biology 209, 221–238.

- Dawes-Hoang, R., Parmar, K., Christiansen, A., Phelps, C. B., Brand, A. H., Wieschaus, E. F., Sep 2005. *folded gastrulation*, cell shape change and the control of myosin localization. *Development* 132 (18), 4165–78.
- Farge, E., 2003. Mechanical Induction of Twist in the *Drosophila* Foregut/Stomodaeal Primordium . *Current Biol.* 13, 1365–1377.
- Gordon, R., 1999. The hierarchical genomes and differentiation waves: novel unification of development, genetics and evolution. ”Singapore & London: World Scientific & Imperial College Press”.
- Grumbling, G., Strelets, V., Consortium, T. F., 2006. Flybase: anatomical data, images and queries. *nucleic acids research* 34: D484-d488; doi:10.1093/nar/gkj068.  
URL <http://flybase.org>
- Hacker, U., Perrimon, N., 1998. DRhoGEF2 encodes a member of the Dbl family of oncogenes and controls cell shape changes during gastrulation in *Drosophila*. *Genes Dev.* 12, 274–84.
- Holzappel, G. A., 2000. Nonlinear solid mechanics. A continuum approach for engineers. J Wiley & Sons Ltd.
- Jacobson, A. G., Oster, G., Odell, G. M., Cheng, L. Y., 1986. Neurotation and the cortical tracting model for epithelial folding. *J. Embryol. Exp. Morph.* 96, 19–49.
- Kam, Z., Minden, J. S., Agard, D. A., Sedat, J. W., Leptin, M., Jun 1991. *Drosophila*, gastrulation: analysis of cell shape changes in living embryos by three-dimensional fluorescence microscopy. *Development* 112 (2), 365–70.
- Leptin, M., 1995. *Drosophila* gastrulation: from pattern formation to morphogenesis. *Annu. Rev. Cell Dev. Biol.* 11, 189–212.
- Leptin, M., 1999. Gastrulation in *Drosophila*: the logic and the cellular mechanisms. *EMBO J.* 18, 3187–3192.
- Leptin, M., Grunewald, B., 1990. Cell shape changes during gastrulation in *Drosophila*. *Development* 110, 72–84.

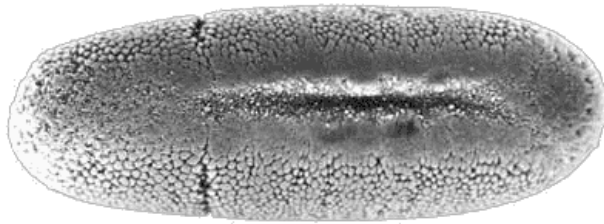
- Muñoz, J., June 2007. Unilateral contact using the null space method and cubic B-spline interpolation. In: CL Bottasso, P Masarati, L. T. (Ed.), *Multibody Dynamics 2007*. Milan, Italy.
- Muñoz, J., Barrett, K., Miodownik, M., 2007. A deformation gradient decomposition method for the analysis of the mechanics of morphogenesis. *J. Biomechanics* 40, 1372–1380.
- Muñoz, J., Jelenić, G., 2004. Sliding contact conditions using the master–slave approach with application on the geometrically non-linear beams. *Int. J. Solids Struct.* 41, 6963–6992.
- Nikolaidou, K. K., Barrett, K., Oct 2004. A Rho GTPase signaling pathway is used re-iteratively in epithelial folding and potentially selects the outcome of Rho activation. *Current Biol.* 14 (20), 1822–6.
- Odell, G. M., Oster, G., Alberch, P., Burnside, B., 1981. The mechanical basis of morphogenesis. I. Epithelial folding and invagination. *Dev. Biology* 85, 446–462.
- Parks, S., Wieschaus, E., Jan 1991. The *Drosophila* gastrulation gene *concertina* encodes a G alpha-like protein. *Cell* 64 (2), 447–58.
- Supatto, W., Débarre, D., Moulia, B., Brozés, E., Martin, J. L., Farge, E., 2005. In *in vivo* modulation of morphogenetic movements in *Drosophila* embryos with femtosecond laser pulses. *Proc. Nat. Acad. Sci. USA* 102 (4), 1047–1052.
- Sweeton, D., Parks, S., Costa, M., Wieschaus, E., 1991. Gastrulation in *drosophila*: the formation of the ventral furrow and posterior midgut invaginations. *Development* 112, 775–789.
- Taber, L. A., 1995. Biomechanics of growth, remodeling, and morphogenesis. *Appl. Mech. Rev.* 48 (8), 487–545.
- Taber, L. A., 2004. *Nonlinear theory of elasticity: applications in biomechanics*. World Scientific Publ.



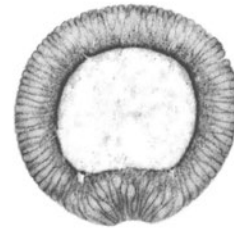
(a)



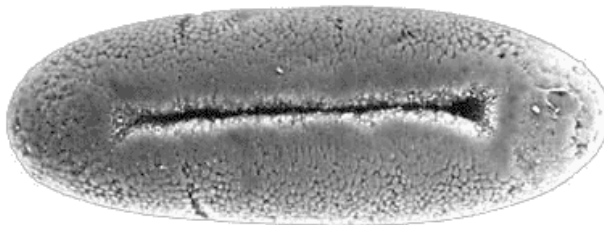
(b)



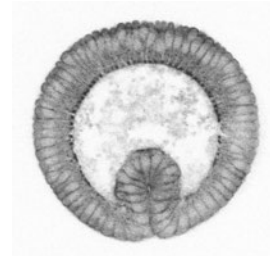
(c)



(d)



(e)



(f)

**Fig. 1. Experimental frames of ventral furrow invagination of the *Drosophila* embryo.** The ventral-furrow primordium appears as a shallow deepening hollow. Images on the left show ventral views (Grumbling et al., 2006) and those on the right a 2D cross-section (Muñoz et al., 2007).

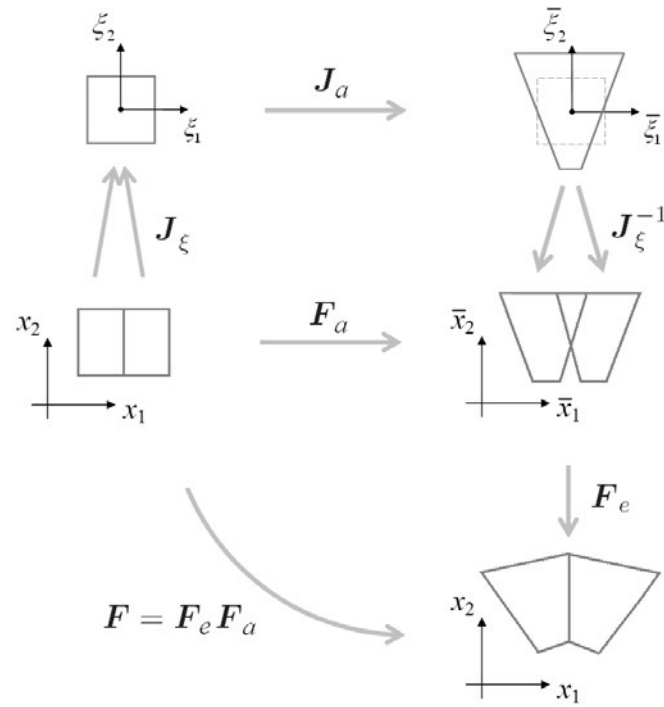
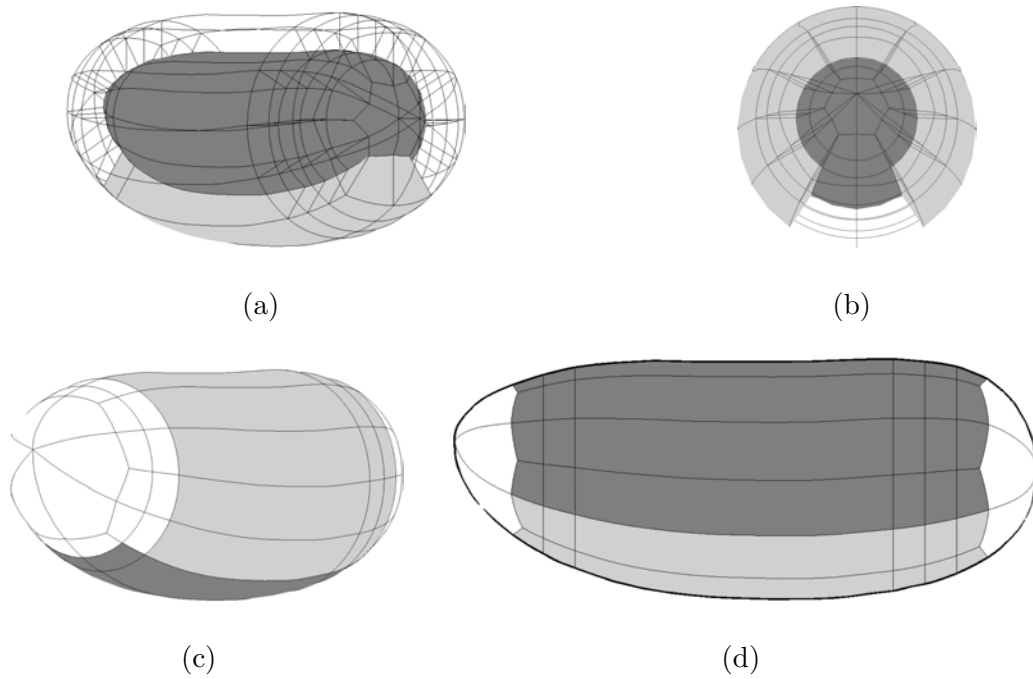


Fig. 2. Scheme of the applied active deformation gradient  $F_a$  within the finite element context.



**Fig. 3. Construction of the 3D Finite Element Model.** (a) Perspective from posterior pole showing active mesodermic domains (light grey) and yolk (dark grey). (b) Anterior view showing active ectodermic domains (light grey) and yolk (dark grey). (c) Schematic of the main three regions of the embryo when the active strains are applied - active radial shortening (light grey), active radial lengthening plus active wedging (dark grey) and no active deformations (white). (d) Lateral view showing arrangement of vitelline membrane - bilateral contact (dark grey) and unilateral contact (light grey).

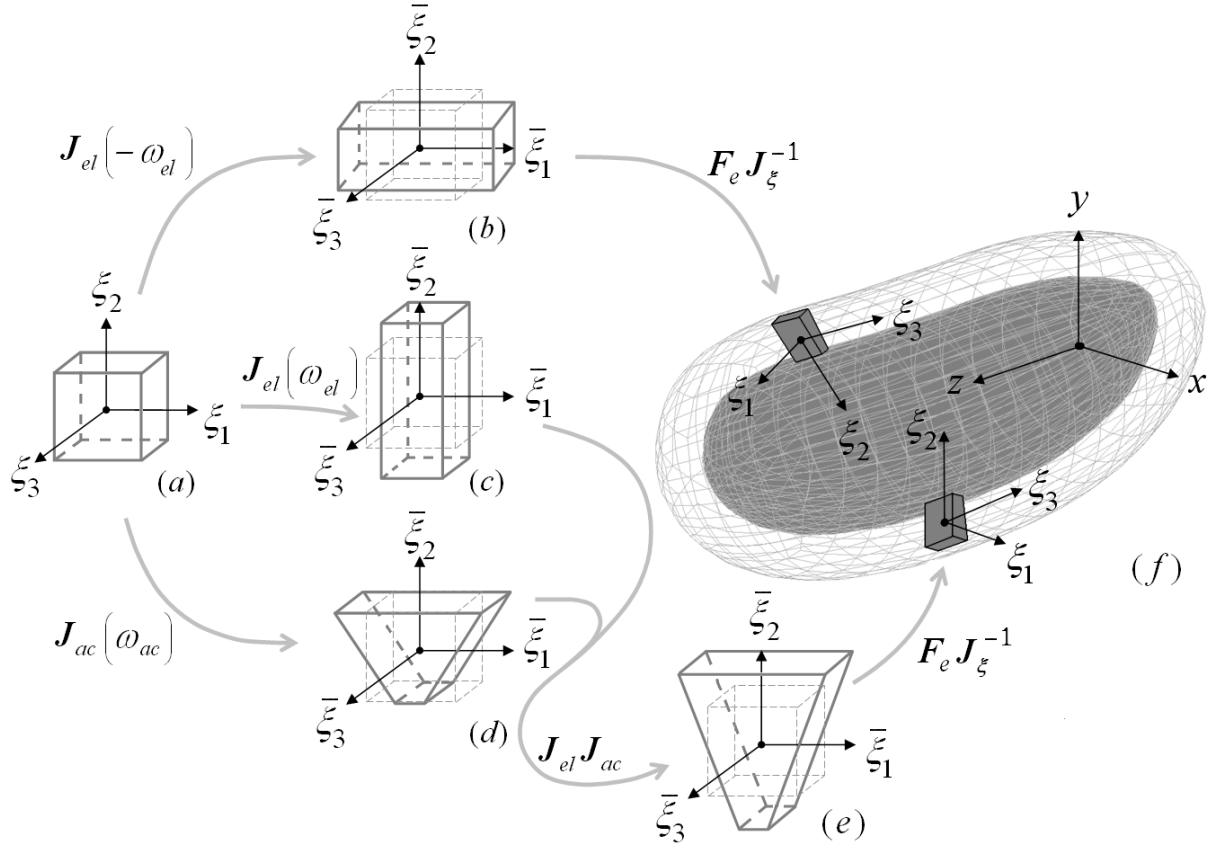


Fig. 4. **Mapping of the active deformations to the finite element geometry.** The pre-established active deformation  $J_a$  of the parent domain is conveyed to each finite element of the discretised geometry through the map  $F_e J_\xi$ ; (a) shows the cubic parent domain common to all the elements of the 3D discretised geometry; (b) shows the active shortening, here applied only to one representative element of the ectodermal region (see Fig.3b). Active radial lengthening (c) is coupled with the active wedging (d), in order to produce the final active deformation (e), which is applied to the elements of the mesodermal region (see Fig.3.a); (f) shows a perspective view of the discretised 3D finite element model in its initial undeformed configuration of reference.

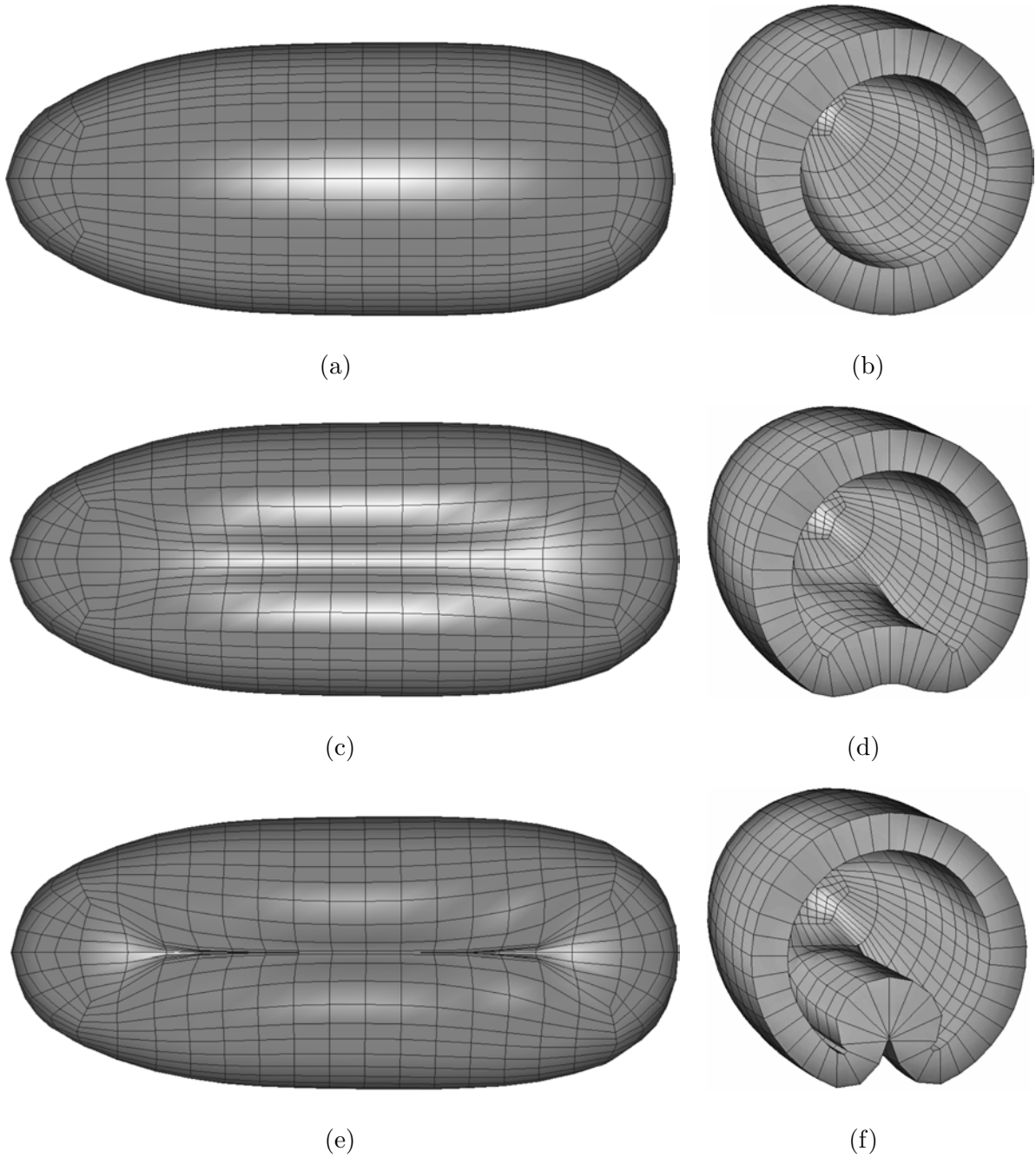


Fig. 5. **Three deformed configurations for  $\alpha = 4$ :** (a) and (b) show respectively a ventral view and a cut-away view of the undeformed finite element model of the embryo in its initial configuration ( $\omega_{ac} = 0$ ,  $\tau = 0$ ), (c) and (d) show a later stage of the simulation in which the embryo model is deformed at  $\omega_{ac} = 0.72$  ( $\tau = 1.2$ ), (e) and (f) show the final stage of the simulation of ventral furrow invagination ( $\omega_{ac} = 1.14$ ,  $\tau = 1.9$ ).

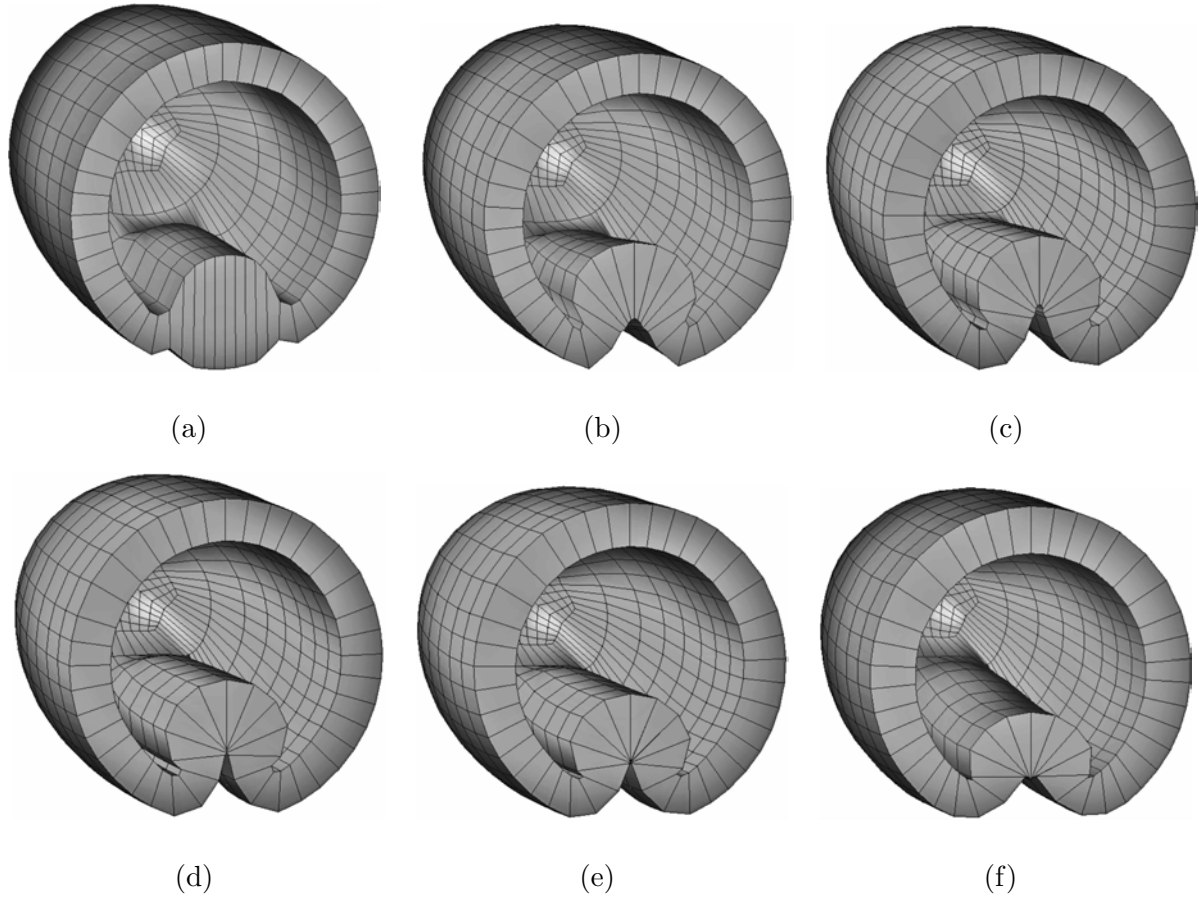


Fig. 6. **3D cut-away views of the invaginated embryo for different values of  $\alpha$ :** the results refer to the final deformations obtained with (a)  $\alpha = 0$ , (b)  $\alpha = 1$ , (c)  $\alpha = 2$ , (d)  $\alpha = 3$ , (e)  $\alpha = 6$ , and (f)  $\alpha = +\infty$ .

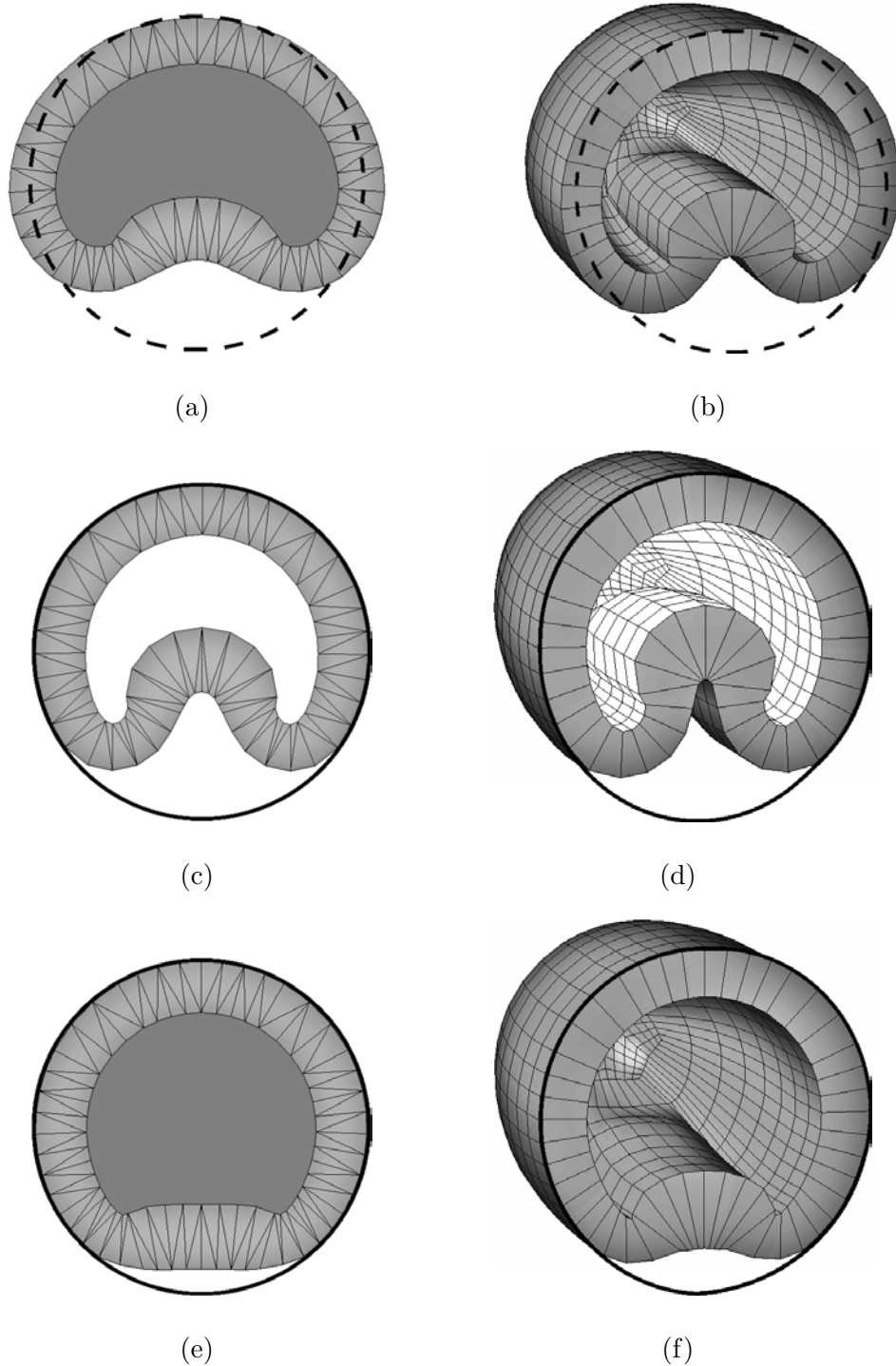


Fig. 7. **Simulations with modified boundary conditions and unusual active deformation:** The figures show simulations where no vitelline membrane is considered (a) 2D section at  $\omega_{ac} = 0.72$ , and (b) 3D view at  $\omega_{ac} = 1.14$ ; where there is no yolk, and therefore no volume constraint (c) 2D section at  $\omega_{ac} = 0.72$  and (d) 3D view at  $\omega_{ac} = 1.14$ ; and finally no ectodermal pushing i.e.  $\omega_{el} = 0$  in the ectodermal regions, (e) 2D section at  $\omega_{ac} = 0.72$  and (f) 3D view at  $\omega_{ac} = 1.14$ . The sections were cut at a distance of approximately  $233 \mu\text{m}$  from the posterior pole, the yolk is highlighted in dark grey.

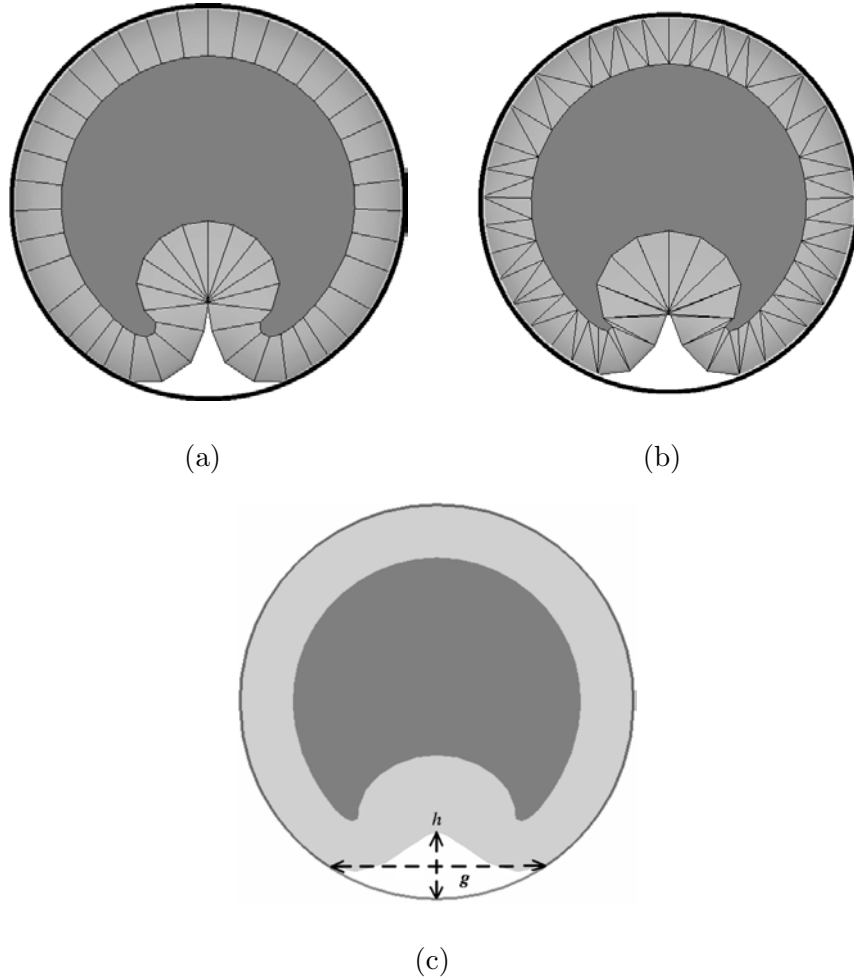


Fig. 8. **Comparison of the 3-D and the 2-D models with  $\alpha = 4$ :** (a) 2D numerical model deformed at  $\omega_{ac} = 1.14$  ( $\tau = 1.9$ ); (b) 3-D section of the model taken a distance of  $233 \mu\text{m}$  from the posterior pole and at  $\omega_{ac} = 1.14$  ( $\tau = 1.9$ ); (c) Schematic illustration of the measurable quantities  $h$  and  $g$  which quantify invagination;

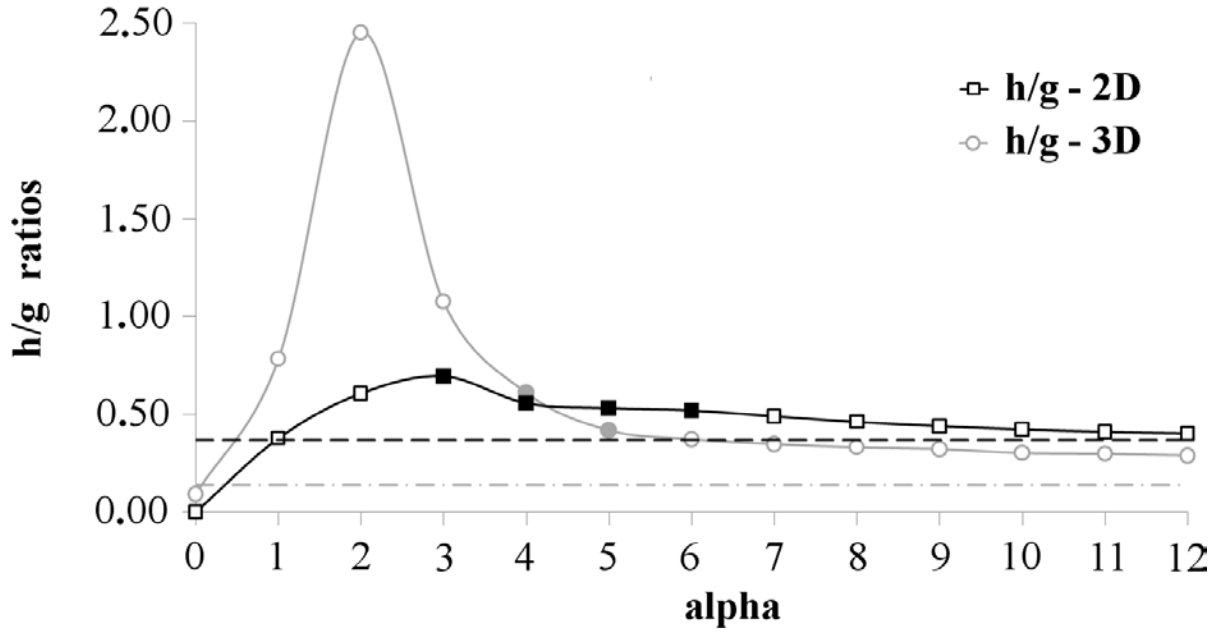
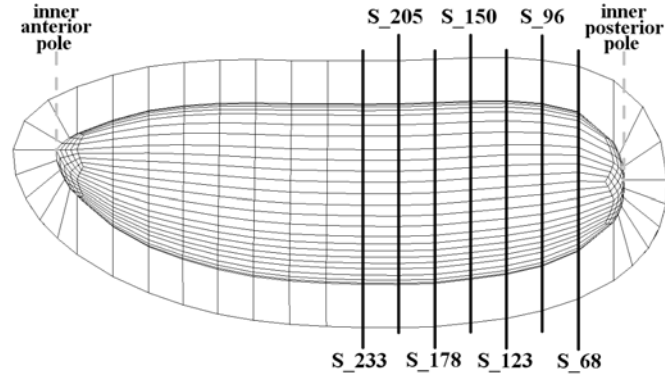
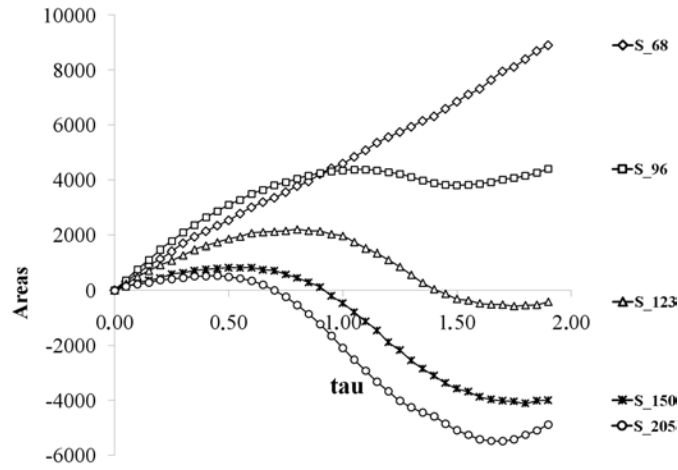


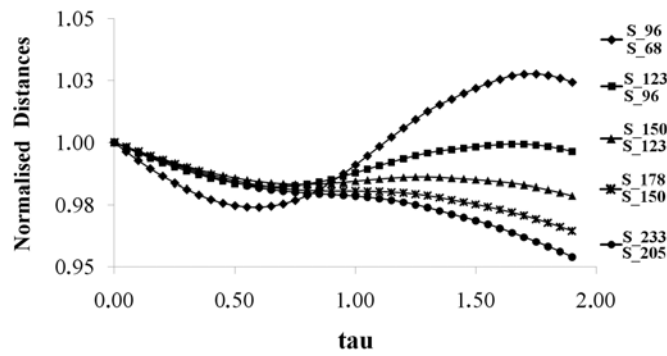
Fig. 9. **Quantitative comparison of the 2D and 3D models:** The ratio of the parameters  $h$  and  $g$  are plotted as a function of  $\alpha$ . The 3D results (black) were measured at the mid-point between the anterior and posterior poles. The limiting values of  $h$  (simple-dash) and  $g$  (dash-dot) at  $\alpha = +\infty$  are also shown. The solid symbols represent data associated with a fully closed ventral furrow.



(a)



(b)



(c)

Fig. 10. **Evolution of the posterior of the embryo during invagination:** (a) Locations of 2D cross-sections along the anterior-posterior axis (the numeric index in the labels of the sections indicates the distance in micron from the posterior pole); (b) the areas of the yolk at these sections as a function of  $\tau$ ; (c) the distances between these sections as a function of  $\tau$ .